Energy 69 (2014) 787–800

Contents lists available at ScienceDirect

Energy

journal homepage: www.elsevier.com/locate/energy

# The phase separation concept condensation heat transfer in horizontal tubes for low-grade energy utilization

Jian Xie, Jinliang Xu*, Feng Xing, Zixuan Wang, Huan Liu

*The Beijing Key Laboratory on Multiphase Flow and Heat Transfer, North China Electric Power University, Beijing 102206, PR China*

ARTICLE INFO

*Article history:*
Received 19 October 2013
Received in revised form
15 March 2014
Accepted 18 March 2014
Available online 14 April 2014

*Keywords:*
Phase separation concept
Condensation heat transfer
Two-phase flow

ABSTRACT

This paper reports condensation heat transfer in a horizontal tube with a 14.81 mm inside diameter and a 1200 mm heat transfer length, by using the phase separation concept. The hollow mesh cylinder was formed by packaging two layers of mesh screen surface. The outer layer had the pore size of 76 μm. This invention constructs a multiscale condenser tube. The modulation of stratified flow and annular flow was focused on. Liquid was held within the mesh cylinder to increase the vapor covered tube wall surface to enhance the heat transfer for stratified flows. For annular flows, liquid droplets in the vapor core were captured by the mesh screen surface to increase the vapor void fractions near the tube wall, enhancing the hat transfer. The measurements showed that the heat transfer coefficients could be more than two times of those in the bare tube. The total thermal resistance was decreased by 45.6%, maximally. The heat transfer enhancement ratios were increased with the vapor mass fluxes, $Gx_{in}$, for the condensation flow along the whole tube length. A pressure analysis explained the increased heat transfer trend. The increment of heat transfer enhancement ratios was suppressed with a liquid flow part in the tube.



## 1. Introduction

The worldwide energy shortage and environment problems demand the energy utilization efficiency to be increased for fossil energy systems. Renewable energy such as solar energy, ocean energy etc. has been put into use. Miniaturization of heat exchangers increases system efficiencies and decreases investment cost. Under many situations, one needs to extract low-grade energy from extremely low temperature resource. An example was cited from Ref. [1]. A heat exchanger for an ocean thermal energy conversion (OTEC) plant required a heat transfer surface area in the order of $10^4$ $m^2$/MW.

The Organic Rankine Cycle (ORC) is a solution to extract low grade heat and convert the heat to power [2–5]. Organic liquid (such as R123) is evaporated to generate vapor, driving the turbine to produce power. The venting vapor at the turbine outlet is condensed in a condenser and circulated by a pump. Enhancement of phase change heat transfer of organic fluid is beneficial to yield more power output and decrease the investment cost.

There is a large amount of waste heat in various industry sectors. The waste heat driven refrigeration or heat pump systems are other effective ways to recover low-grade heat [6–8]. An important technical barrier to expand the waste heat utilization is the large component/system size and high investment cost. The evaporator and condenser are necessary in these systems. Organic fluids have been frequently used due to their low saturation temperatures. However, organic fluids have lower specific heats, thermal conductivities and latent heat of evaporation compared with water. The phase change heat transfer coefficients of organic fluids are even lower than the forced convective heat transfer coefficients of water [9]. The low-grade energy utilization requires significant reduction of the component size and investment cost with new phase change heat transfer concept or technique.

Condensation heat transfer can be enhanced by microstructures on the tube wall. Microgroove tubes (Graham et al. [10]), micro-fin tubes (Cavallini et al. [11]), herringbone tubes (Miyara and Otsubo [12]), helically corrugated tubes (Laohalertdecha and Wongwises [13]) belong to the enhanced condenser tubes. Heat transfer enhancement mechanism is attributed by mixing the fluid boundary layers and limiting the growth of fluid boundary layers close to the tube wall.

Many authors explained the heat transfer coefficients dependent on the two-phase distribution in tubes. Previous studies focused on the flow patterns with condensation in inclined tubes. Nitheanandan and Soliman [14] investigated the tube inclination effect on the flow regime boundaries during condensation of steam.

* Corresponding author. Tel./fax: +86 10 61772058.
*E-mail address:* xjl@ncepu.edu.cn (J. Xu).

http://dx.doi.org/10.1016/j.energy.2014.03.075
0360-5442/

**Nomenclature**

| | |
|---|---|
| BT | bare tube |
| $C_p$ | specific heat at constant pressure, J/kg K |
| $D$ or $d$ | diameter, m |
| $D_\sigma$ | distance between two mesh wires, m |
| EF | heat transfer enhancement ratio |
| $F_{\sigma\tilde{i}}$ | capillary forced created by the mesh p $\tilde{k}$ ore, N |
| $F_{\sigma\tilde{k}}$ | capillary force for the array shaded in the gravity direction, N |
| $g$ | acceleration of gravity, m/s$^2$ |
| $G$ | mass flux, kg/m$^2$s |
| $h$ | heat transfer coefficient, W/m$^2$ K |
| $\tilde{h}$ | the liquid height, m |
| $i$ | enthalpy, J/kg |
| $\tilde{i}$ | width array in Fig. 5 |
| $i_{fg}$ | latent heat of evaporation, J/kg |
| $I$ | current, A |
| $\tilde{I}$ | maximum width array in Fig. 5 |
| $\tilde{j}$ | array in gravity direction |
| $\tilde{J}$ | maximum array in gravity direction |
| $k$ | thermal conductivity, W/(m K) |
| $\tilde{k}$ | circumference array |
| $\tilde{K}$ | maximum circumference array |
| $L$ | length, m |
| LMTD | logarithmic mean temperature difference, °C or K |
| $m$ | mass flow rate, kg/s |
| $\tilde{m}$ | mass, kg |
| $n$ | total number of cross-sections divided along the flow direction |
| $P$ | pressure, Pa |
| $\Delta P_f$ | frictional pressure drop, Pa |
| PEC | performance evaluation number |
| PPI | pores per inch |
| $q$ | heat flux on the inner wall surface, W/m$^2$ |
| $Q$ | heat transfer rate or heat transfer rate per unit flow length, W or W/m |
| $r$ | radius coordinate, m |
| $R$ | thermal resistance, K/W |
| $\tilde{R}$ | mesh cylinder radius, m |
| $S$ | circumference, m |
| $t$ | time, s |
| $T$ | temperature, °C or K |
| $\Delta T$ | temperature difference between the vapor and tube wall, °C or K |
| $\Delta T_c$ | temperature rise of the cooling water in the tube annulus, °C or K |
| $U$ | voltage, V |
| $u$ | axial velocity, m/s |
| $w$ | mesh pore width, m |
| $x$ | vapor mass quality |
| $\tilde{x}_1, \tilde{x}_2, \tilde{x}_3 \ldots \tilde{x}_n$ | independent variables |
| $\Delta\tilde{x}_1, \Delta\tilde{x}_2, \Delta\tilde{x}_3 \ldots \Delta\tilde{x}_n$ | uncertainties of independent parameters |
| $Y$ | any dependent variable |
| $\Delta Y$ | uncertainties of the dependent parameter |
| $z$ | axial coordinate, m |

*Greek symbols*

| | |
|---|---|
| $\alpha$ | contact angle between the gas–liquid interface and the mesh wire |
| $\beta$ | angle of the line $OO'$ with respect to the gravity direction (see Fig. 5c) |
| $\delta_{mesh}$ | mesh wire thickness, m |
| $\theta$ | total arc angle for the settled liquid within the mesh cylinder |
| $\eta$ | thermal efficiency |
| $\rho$ | density, kg/m$^3$ |
| $\sigma$ | surface tension, N/m |
| $\Delta$ | liquid film thickness along the axial direction, m |
| $\phi_{lo}^2$ | two-phase flow multiplier |

*Subscript*

| | |
|---|---|
| 1 | evaporator inlet |
| 2 | evaporator outlet |
| an | annular region |
| ave | average |
| b | bottom wall location |
| BT | bare tube |
| c | cooling water |
| cy | mesh cylinder |
| co | core region |
| con | condenser |
| e | exit |
| eff | effective heat transfer |
| eq | equilibrium |
| eva | evaporator |
| film | film condensation |
| $i$ | the cross-section number along the flow direction |
| ins | inside wall surface |
| in | condenser inlet |
| l | liquid |
| max | maximum |
| min | minimum |
| MHTT | modulated heat transfer tube |
| o | outer wall surface |
| out | condenser outlet |
| r | organic fluid (R123 in this study) |
| s | side wall location |
| SP | single-phase flow |
| t | top wall location |
| to | total |
| TP | two-phase flow |
| u | upstream |
| v | vapor |
| w | wall |

They used a 13.4 mm inner diameter copper tube with small inclination angles (from 10° downwards to 10° upwards). It was found that influence of the inclination angle on the annular flow regime boundary was almost insignificant. However, even a small inclination angle had a strong influence on wavy and slug flow regime boundaries.

Lips and Meyer [15] examined the effect of inclination angles on the convective condensation in a smooth tube. They showed that heat transfer coefficient was strongly affected by the liquid and vapor distributions and especially by the liquid layer thickness at the tube bottom for stratified flows. Thus developing a mechanistic model of flow pattern maps was necessary in achieving a predictive tool for the heat transfer coefficient in convective condensation in inclined tubes.

Recently, Chen et al. [16] proposed the phase separation concept to modify flow patterns in a tube. An empty mesh cylinder was

suspended in the tube. Mesh pores prevented gas bubbles from entering the mesh cylinder but captured liquid into the mesh cylinder, increasing void fractions near the tube wall and yielding thin liquid films on the wall. An adiabatic air–water two-phase flow experiment was performed to verify the idea. The modulation of intermittent (bubbly/slug/plug) flows was focused on.

Subsequently, Chen et al. [17] performed the numerical simulation of flow pattern modulations for air–water vertical upflows. The results did show the zero void fractions inside the mesh cylinder and higher void fractions near the tube wall. Liquid film thicknesses in the modulated flow section were 1/6–1/3 of those in the bare tube section. Besides, three-levels of liquid circulation were identified to promote the liquid mixing over the whole tube length and within the radial direction.

Our previous flow pattern modulation studies were performed for adiabatic air–water flows focusing on the intermittent flows. Here we report the modulated condensation heat transfer for the first time. The modulation of phase change heat transfer in an organic fluid system is a challenge issue. The phase separation is due to the capillary separation by the micro-membrane surface. The surface tension ($\sigma$) of the organic fluid such as R123 is only 1/6–1/7 of that for water. This paper is organized as follows. Section 2 describes the experimental details. Section 3 describes the results and discussion, consisting of four subsections. Section 3.1 reports the visualization results. Section 3.2 demonstrates the heat transfer measurement results. Section 3.3 analyzes the increase trend of the heat transfer enhancement with the vapor mass fluxes. Section 3.4 comments on the penalty of the pressure drop increase. Major conclusions are summarized in Section 4.

## 2. Experimental setup

### 2.1. Experimental loop

Fig. 1 shows the experimental setup. The system consisted of an organic fluid loop, an evaporator section, a test section, a chiller water loop, a tap water cooled post-condenser and relevant instruments. The organic fluid loop circulated the R123 fluid. Initially the loop was vacuumed to remove the non-condensable gas and then was charged by the R123 liquid. The R123 liquid was stored in a reservoir. A piston pump provided the R123 flow rate to the loop. A bypass line connected the pump inlet and outlet. An accumulator was installed at the pump outlet to stabilize the fluid pressure. The accumulator had a specific liquid level, which was pressurized by the nitrogen gas. An oil separator collected the oil droplet and prevented the oil from entering the test section.

The evaporating section was a helical-coiled tube heated by an AC (alternative current) electrical power. A transformer converted high voltage to low voltage. Two copper plates were welded on the curved tube and acted as the electrodes. The evaporating section was electrically insulated with other components of the loop. The curved tube was wrapped by the thick thermal insulation material. The power was obtained by the measured voltage and current. The inlet of the evaporating section was the subcooled liquid with the temperature of $T_{r,1}$. The outlet temperature was $T_{r,2}$. The two-phase state at the outlet caused that $T_{r,2}$ was equal to the fluid saturation temperature. The test section was exactly horizontally positioned. A bare tube (called BT) and a modulated heat transfer tube (called MHTT with a mesh cylinder insert) were tested.

The two-phase mixture in the test section was condensed by the chiller water loop, which included a chiller, a mass flow meter and two jacket thermocouples. The chiller generated a stable chiller water flow rate, $m_c$, measured by a mass flow meter. The heat was dissipated by a fan to the ambient air. Two thermocouples ($T_{c,in}$ and $T_{c,out}$) measured the inlet and outlet temperatures of the chiller water. The post-condenser further condensed the two-phase mixture to a subcooled liquid state. A regulating valve precisely adjusted the tap water flow rate.

### 2.2. Test section

The test section was a counter-current condenser (see Fig. 2), consisting of two sight glass tube adaptors, an inner copper tube and an outer stainless steel tube. Two flanges connected the copper tube and the sight glass tube together. The copper tube had an outer diameter of 18.97 mm with the thickness of 2.08 mm. It had an inner diameter of 14.81 mm, with the heat transfer length of 1200 mm. The 304 stainless steel tube had an inner diameter of 23.80 mm, forming a tube annulus of 2.41 mm.

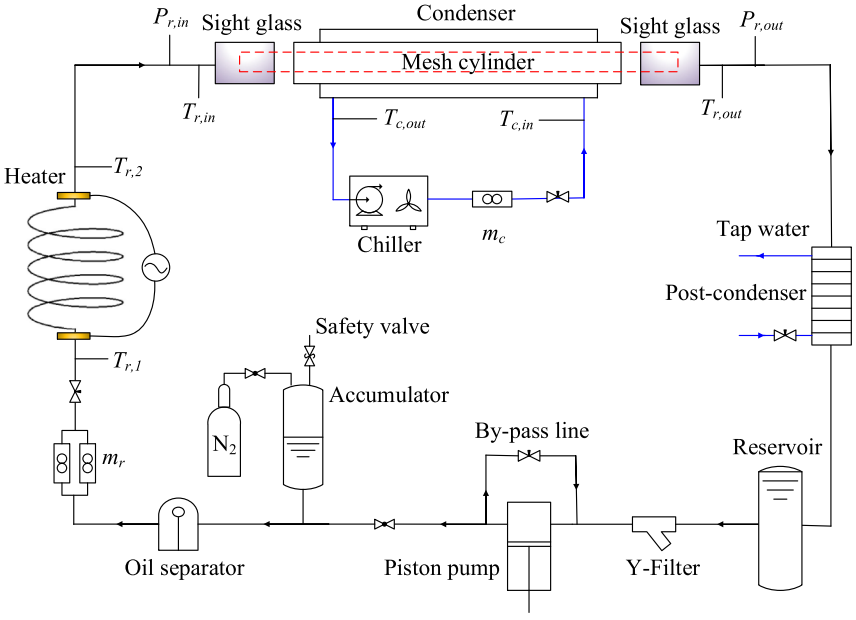


**Fig. 1.** The experimental setup.

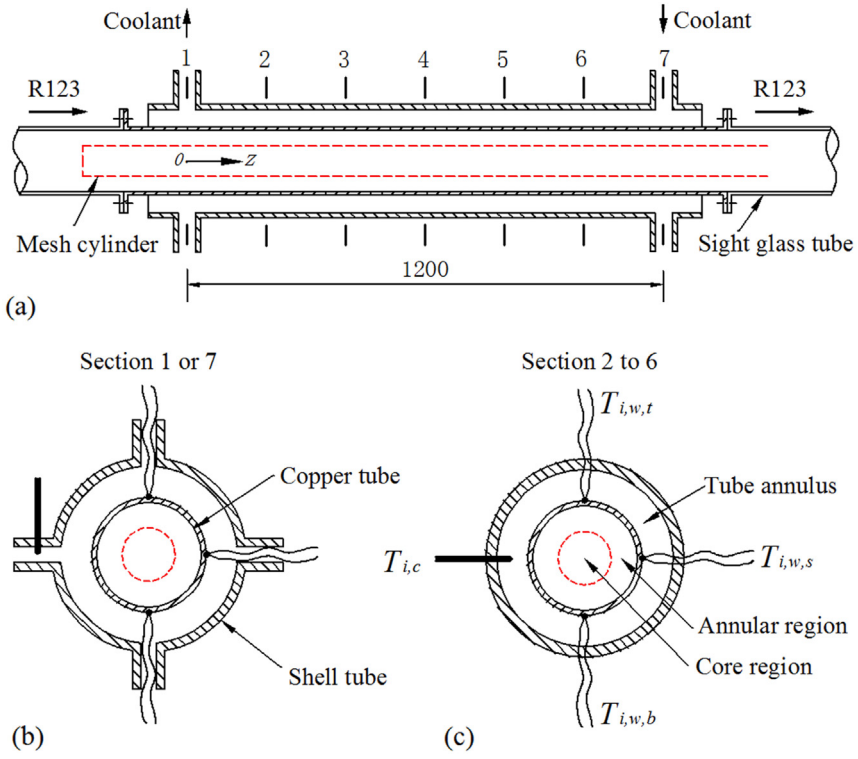


**Fig. 2.** The modulated heat transfer tube (MHTT) with water cooling in the tube annulus.

Seven cross-sections were marked as 1–7. The cross-sections 1 and 7 were for the organic fluid inlet and outlet, respectively (see Fig. 2b). Four branch tubes were welded with the outer stainless steel tube to vent the cooling water in the tube annulus. Three thermocouple wires were welded on the top, side and bottom wall locations. The thermocouple wires penetrated the corresponding branch tube for signal processing. A jacket thermocouple near the junction of the branch tube and the stainless steel tube measured the cooling water temperature. The cross-sections 2–6 did not contain the branch tube. The three thermocouples on the tube wall were marked as $T_{i,w,t}$, $T_{i,w,s}$ and $T_{i,w,b}$, where $i$ refers to the cross-section number ($i = 2$–6), $w$ refers to the wall, t, s and b refers to the top, side and bottom locations, respectively. $T_{i,c}$ measured the cooling water temperature in the tube annulus with c standing for the cooling water. Inserting a mesh cylinder in the tube divided the tube cross-section into a core region and an annular region (see Fig. 2c). The BT (by that in the bare tube) was exactly the same as the MHTT, except that it did not contain the mesh cylinder insert.

The mesh cylinder had a length of 1698 mm (longer than 1200 mm). Thus, the mesh cylinder inlet and outlet parts could be seen through the sight glass tubes. Fig. 3a shows the fabricated mesh cylinder, which was made of a rough inner layer and a fine outer layer of mesh screens. The inner layer had the PPI (pores per inch) of 80, mesh wire thickness of 130 μm and mesh pore width of 194 μm. The inner mesh layer increased the mesh cylinder hardness so that the mesh cylinder was not deformed. The outer layer had the PPI of 200 with the mesh pore width of 76 μm and mesh wire thickness of 46 μm (see Fig. 3b–c). The two layers were packaged to have a thickness of 0.76 mm. Table 1 summarizes the major parameters.

### 2.3. Calibration experiment

Because the two-phase mixture enthalpy cannot be determined by its temperature alone, the single-phase liquid flow and heat transfer experiments were performed to obtain the evaporator and condenser efficiencies. The evaporator thermal efficiency with R123 liquid was

$$\eta_{\mathrm{eva}} = \frac{m_{\mathrm{r}} C_{\mathrm{p,r}} (T_{\mathrm{r},2} - T_{\mathrm{r},1})}{UI} \tag{1}$$

where $m_{\mathrm{r}}$ was the R123 mass flow rate, $C_{\mathrm{p,r}}$ was the specific heat of R123 liquid, $T_{\mathrm{r},2}$ and $T_{\mathrm{r},1}$ were the liquid temperatures at the evaporator inlet and outlet respectively, $U$ was the voltage and $I$ was the current. The measured thermal efficiency was in the range of 0.95–0.99. Thus, the evaporator thermal efficiency was set as 0.97.

Then, the condenser thermal efficiency (organic fluid side), $\eta_{\mathrm{con}}$, was

$$\eta_{\mathrm{con}} = \frac{m_{\mathrm{c}} C_{\mathrm{p,c}} (T_{\mathrm{c,out}} - T_{\mathrm{c,in}})}{m_{\mathrm{r}} C_{\mathrm{p,r}} (T_{\mathrm{r,in}} - T_{\mathrm{r,out}})} \tag{2}$$

where $m_{\mathrm{c}}$ was the cooling water mass flow rate, $C_{\mathrm{p,c}}$ was the water specific heat, $T_{\mathrm{c,out}}$ and $T_{\mathrm{c,in}}$ were the outlet and inlet water temperatures, respectively. The measured $\eta_{\mathrm{con}}$ reached about 0.98.

We also measured the friction factors and Nusselt number for the single-phase liquid flow in the bare tube. The measured friction factors in the turbulent liquid flow regime agreed well with those computed by the Blasius expression [18], with the difference between them less than 8.07%. The measured Nusselt number also matched the Dittus–Boelter correlation [19] well, with the relative difference less than 6.39%.

### 2.4. Data reduction and uncertainty analysis

#### 2.4.1. Inlet and outlet vapor qualities ($x_{in}$ and $x_{out}$)

The condenser inlet enthalpy, $i_{\mathrm{r,in}}$, and quality, $x_{\mathrm{in}}$, were based on the measured parameters in the evaporator and the calibrated evaporator efficiency, $\eta_{\mathrm{eva}}$ (see Section 2.3):

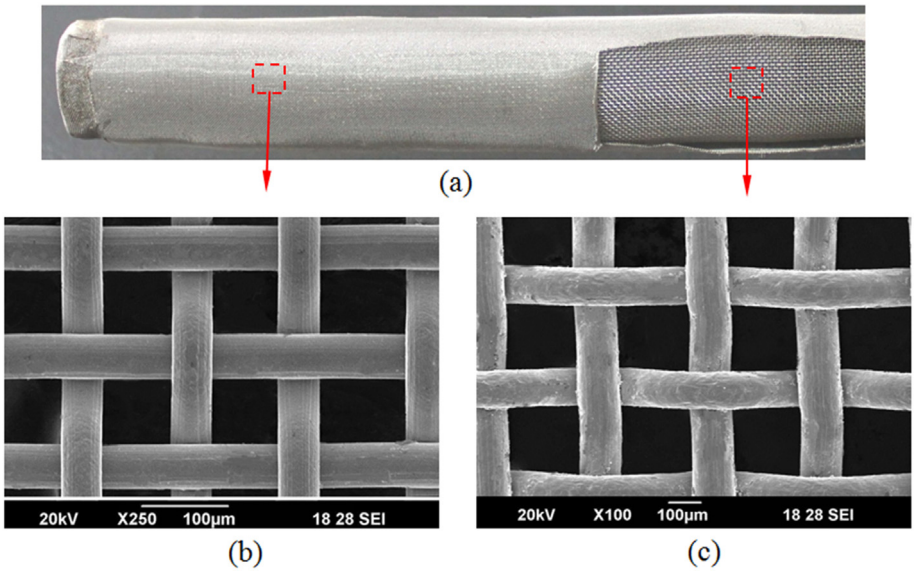


**Fig. 3.** The fabricated mesh cylinder to be inserted in the tube (a) and the SEM images of the mesh screen for the outer layer with PPI = 200 and $w$ = 76 μm (b) and the inner layer with PPI = 80 and $w$ = 194 μm (c).

$$i_{r,in} = i_{r,1} + \frac{UI\eta_{eva}}{m_r} \tag{3}$$

$$x_{in} = \frac{i_{r,in} - i_{l,in}}{i_{fg,in}} \tag{4}$$

where $i_{r,1}$ is the R123 enthalpy at the evaporator inlet, $i_{l,in}$ is the R123 saturated liquid enthalpy, $i_{fg}$ is the latent heat of evaporation.

Similarly, the condenser efficiency ($\eta_{con}$ in Eq. (2)) was used to compute the condenser outlet parameters. The heat received by the cooling water in the tube annulus was

$$Q = m_c C_{p,c}(T_{c,out} - T_{c,in}) \tag{5}$$

The heat flux based on the inner tube wall surface of the copper tube was

$$q = Q\Big/\left(\pi d_{ins} L_{eff}\right) \tag{6}$$

where $L_{eff}$ is the effective heat transfer length. The outlet vapor enthalpy and quality were

$$i_{r,out} = i_{r,in} - Q/m_r \tag{7}$$

$$x_{out} = \frac{i_{r,out} - i_{l,out}}{i_{fg,out}} \tag{8}$$

**Table 1**
The major parameters of components for the test section.

| Components | Materials | Parameters |
|---|---|---|
| Shell tube | 304 stainless steel | $D_{ins}$ = 23.80 mm, $D_o$ = 30.00 mm |
| Copper tube | T2 type copper | $d_{ins}$ = 14.81 mm, $d_o$ = 18.97 mm, $L_{eff}$ = 1200 mm |
| Mesh cylinder | 316 stainless steel | $D_{cy}$ = 11.20 mm, $L_{cy}$ = 1698 mm |
| Outer mesh screen layer | 316 stainless steel | PPI = 200, $w$ = 76 μm, $\delta_{mesh}$ = 46 μm |
| Inner mesh screen layer | 316 stainless steel | PPI = 80, $w$ = 194 μm, $\delta_{mesh}$ = 130 μm |
| Sight glass tube | transparent quartz | $D$ = 15.80 mm, $L$ = 200 mm |

where $i_{l,out}$ and $i_{fg,out}$ are the saturated liquid enthalpy and latent heat of evaporation based on the outlet pressure, respectively.

*2.4.2. Thermal resistance and heat transfer coefficient*

The total condenser thermal resistance included the condensation thermal resistance, $R_r$, the thermal conduction thermal resistance $R_w$, and the cooling water resistance in the tube annulus, $R_c$:

$$R_{to} = R_r + R_w + R_c \tag{9}$$

$$R_{to} = \frac{1}{\pi d_{ins} L_{eff} h_{to}}, \quad R_r = \frac{1}{\pi d_{ins} L_{eff} h}, \quad R_w = \frac{\ln(d_o/d_{ins})}{2\pi L_{eff} k_w}, \quad R_c = \frac{1}{\pi d_o L_{eff} h_c} \tag{10}$$

where $h_{to}$, $h$, $h_c$ are the heat transfer coefficients of total, condensation, and cooling water, respectively, $d_{ins}$ and $d_o$ are the inside and outside diameters of the copper tube. Thus, $h$, was

$$h = \frac{1}{\frac{1}{h_{to}} - \frac{d_{ins}}{2k_w}\ln\left(\frac{d_o}{d_{ins}}\right) - \frac{d_{ins}}{d_o}\frac{1}{h_c}} \tag{11}$$

The total heat transfer coefficient $h_{to}$ in Eq. (11) was

$$h_{to} = \frac{q}{\mathrm{LMTD}} \tag{12}$$

In which $q$ was predicted by Eqs.(5) and (6), the LMTD temperature difference was

$$\mathrm{LMTD} = \frac{(T_{r,in} - T_{c,out}) - (T_{r,out} - T_{c,in})}{\ln\left(\frac{T_{r,in} - T_{c,out}}{T_{r,out} - T_{c,in}}\right)} \tag{13}$$

$$h_c = \frac{q d_{ins}}{d_o(T_{w,ave} - T_{c,ave})} \tag{14}$$

$T_{w,ave}$ and $T_{c,ave}$ are the average temperatures of the tube wall and the cooling water, which are

$$T_{w,ave} = \frac{1}{3n}\sum_{i=1}^{n} T_{i,w,t} + T_{i,w,s} + T_{i,w,b}, \quad T_{c,ave} = \frac{1}{n}\sum_{i=1}^{n} T_{i,c} \tag{15}$$

The subscripts t, s and b refer to the top, side and bottom wall (see Fig. 2c), $i$ is the cross-section number, $n$ equals to 7 here.

*2.4.3. Heat transfer enhancement ratio and PEC number*

The heat transfer enhancement ratio was defined as the condensation heat transfer coefficient in the modulated heat transfer tube (MHTT) divided by that in the bare tube (BT), $EF = h_{MHTT}/h_{BT}$. It is noted that EF is a global parameter over the whole heat transfer length. EF should be larger in the tube entrance part and will be decreased along the flow length. The PEC number characterized the heat transfer enhancement relative to the pressure drop increase penalty:

$$PEC = \frac{h_{MHTT}/h_{BT}}{\left(\Delta P_{f,MHTT}/\Delta P_{f,BT}\right)^{0.1667}} \tag{16}$$

The heat transfer device is recommended to be used when the PEC number is larger than one [20,21]. The frictional pressure drop in Eq. (16) came from the measured pressure drop subtracting the acceleration pressure drop computed by Tran [22]. This study covered the following parameter ranges: $P_{r,in} = 250 \pm 5$ KPa, $T_{r,in} = 55 \pm 0.5$ °C, $G = 100$–$500$ kg/m$^2$s, $x_{in} = 0.042$–$0.934$ for R123, and $T_{c,in} = 25 \pm 0.3$ °C, $m_c = 300$–$700$ kg/h for the cooling water.

High accuracy sensors and instruments were used. For instance, the OMEGA K-type thermocouples and DMF-1-DX mass flow meter were used for temperature and mass flow rate measurements. The standard calibration procedures were performed before the formal experiment. The temperatures and mass flow rate had the uncertainties of 0.2 °C and 0.1%, respectively. The heat transfer coefficient, thermal resistance and *PEC* values were determined by a set of measured parameters. The uncertainties of these parameters were evaluated based on the error transmission theory [23]. If $Y$ is a given function of the independent variables of $\tilde{x}_1, \tilde{x}_2, \tilde{x}_3, \ldots \tilde{x}_n$, and $\Delta\tilde{x}_1, \Delta\tilde{x}_2, \Delta\tilde{x}_3, \ldots \Delta\tilde{x}_n$ are the uncertainties of these independent parameters, the uncertainty of $Y$ is

$$\Delta Y = \sqrt{\left(\frac{\partial Y}{\partial \tilde{x}_1}\Delta\tilde{x}_1\right)^2 + \left(\frac{\partial Y}{\partial \tilde{x}_2}\Delta\tilde{x}_2\right)^2 + \ldots \left(\frac{\partial Y}{\partial \tilde{x}_n}\Delta\tilde{x}_n\right)^2} \tag{17}$$

Finally, the heat transfer coefficient, enhanced heat transfer ratio and PEC values had the uncertainties of 2.37–12.62%, 3.73–17.07% and 3.89–17.01%, respectively. The errors of these parameters strongly depended on the temperature difference between the tube wall and fluid. At the small temperature difference, the uncertainties were larger. The uncertainties were decreased with increases in the temperature difference. Table 2 summarizes the uncertainties.

**Table 2**
The major parameters, instruments and uncertainties.

| Parameters | Instruments | Uncertainties |
|---|---|---|
| Wall temperature | K-type thermocouple wire | 0.2 °C |
| Fluid temperature | K-type jacket thermocouple | 0.2 °C |
| R123 mass flow rate | DMF-1-DX mass flow meter | 0.1% |
| Cooling water mass flow rate | DMF-1-DX mass flow meter | 0.1% |
| Pressure | Rosemount-3051 pressure transducer | 1.0% |
| $h$ | | 2.37–12.62% |
| EF | | 3.73–17.07% |
| PEC | | 3.89–17.01% |

## 3. Results and discussion

### 3.1. Flow consideration

*3.1.1. Direct flow observation*

Flow patterns were observed through the entrance sight glass tube. The mass flux, $G$, and the inlet vapor quality, $x_{in}$, characterized the flow patterns. The stratified smooth flow (SS), stratified wavy flow (SW) and annular flow ($A$) in the bare tube were observed. The bubbly flow and slug flow were not observed. Many refrigerant condensation flow pattern maps were reported [24–26], for which the inside tube diameter was 8.0 mm thus the surface tension force still played important role to form the bubble flow and slug flow.

Fig. 4 shows the flow pictures. For the SS and SW flows, the mesh cylinder modulated the flows to have two transparent liquid levels: the liquid level $a$ in the core region and the liquid level $b$ in the annular region (see Fig. 4). At $G = 199$ kg/m$^2$s and $x_{in} = 0.103$, the liquid level in the bare tube was 7.13 mm and the vapor covered tube surface area per unit flow length was 0.0264 m$^2$/m. When the same flow interacted with the mesh cylinder, the liquid level $a$ was increased to 8.02 mm with the liquid level $b$ of 4.15 mm, yielding the vapor covered tube surface area of 0.0326 m$^2$/m, which was increased by 23.5% compared with the bare tube to enhance the heat transfer.

*3.1.2. Stratified flow pattern modulation analysis*

The mesh cylinder consisted of a side mesh screen surface (A–A cross-section) and a circular mesh cylinder surface (B–B cross-section, see Fig. 5a). Over the A–A cross-section, each mesh pore is numbered as $(\tilde{i},\tilde{j})$ with $\tilde{i}$ as the width array and $\tilde{j}$ as the gravity array (see Fig. 5b). The capillary forced created by the mesh pore $(\tilde{i}, 1)$ is

$$F_{\sigma\tilde{i}} = \pi\sigma w \sin\alpha \tag{18}$$

where $w$ is the mesh pore width and $\alpha$ is the contact angle between the gas–liquid interface and the mesh wire. $F_{\sigma\tilde{i}}$ should be balanced by the total gravity force over the mesh pores $(\tilde{i},\tilde{j})$ with $\tilde{j}$ from 1 to $\tilde{J}$:

$$F_{\sigma\tilde{i}} = \sum_{\tilde{j}=1}^{\tilde{J}} \tilde{m}_{(\tilde{i},\tilde{j})} g \tag{19}$$

Combining Eqs. (18) and (19) yields

$$\pi\sigma w \sin\alpha = \rho_l g w^2 \tilde{J}\Delta \tag{20}$$

where $\Delta$ is the liquid thickness surrounding the mesh pores along the axial flow direction $z$

$$\Delta = \frac{\pi\sigma\sin\alpha}{\rho_l g w \tilde{J}} \tag{21}$$

Fig. 5c shows the phase distribution (B–B cross-section). Along the circumference direction, the array is marked as $\tilde{k}$ from 1 to $\tilde{K}$(the maximum $\tilde{k}$ array). The total arc angle for the settled liquid within the mesh cylinder is $\theta$. For the array $\tilde{k}$, the angle of the line $OO'$ with respect to the gravity direction is $\beta$, in which $O$ is the tube center point and $O'$is the center point of two mesh wires (see Fig. 5c).

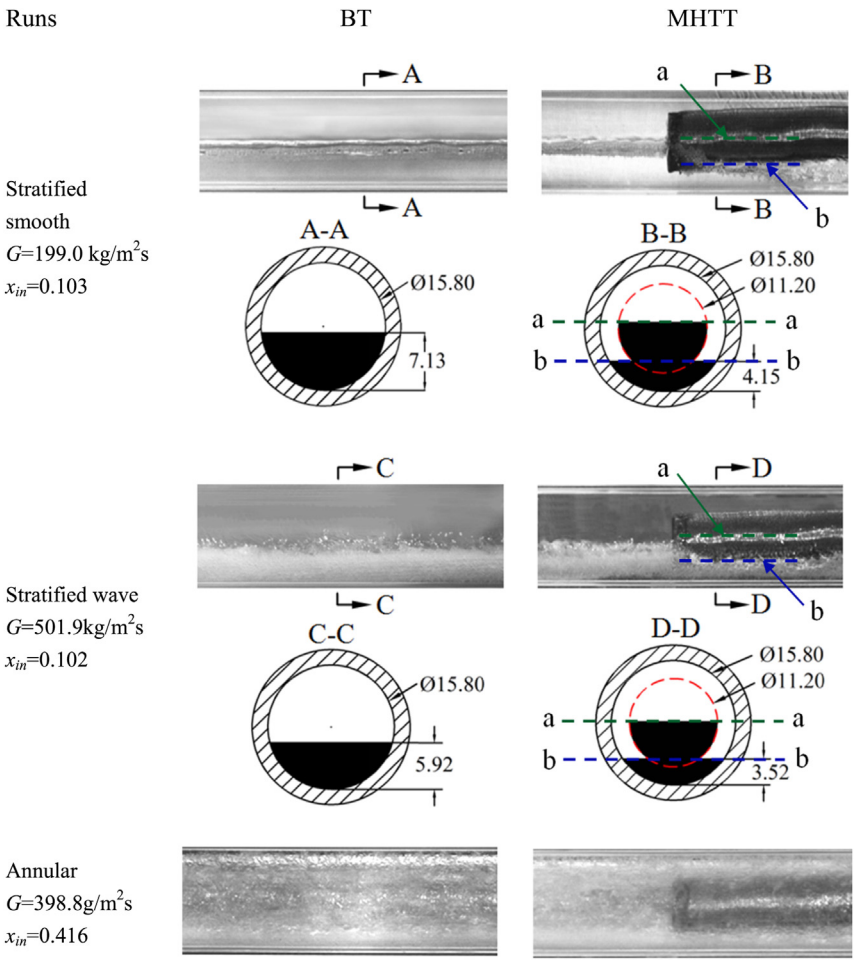


**Fig. 4.** The flow patterns in the bare tube and those observed through the sight glass tube with mesh cylinder inset.

$$\beta = \frac{\theta}{2\tilde{K}} + \left(\frac{\theta}{2} - \frac{\tilde{k}\theta}{\tilde{K}}\right) \tag{22}$$

The distance between two mesh wires is $D_\sigma$:

$$D_\sigma = 2\tilde{R}\sin\left(\frac{\theta}{2\tilde{K}}\right) \tag{23}$$

The capillary force for the array $\tilde{k}$ shaded in the vertical (gravity) direction is

$$F_{\sigma\tilde{k}} = 2\pi\tilde{R}\sigma\sin\alpha\sin\left(\frac{\theta}{2\tilde{K}}\right)\cos\left(\frac{\theta}{2\tilde{K}} + \left[\frac{\theta}{2} - \frac{\tilde{k}\theta}{\tilde{K}}\right]\right) \tag{24}$$

where $\tilde{R}$ is the mesh cylinder radius. $F_{\sigma\tilde{k}}$ is balanced by the gravity force over the unit marked by the dashed lines (see Fig. 5c). $F_{\sigma\tilde{k}}$ is the force to hold higher liquid level in the mesh cylinder. If $F_{\sigma\tilde{k}}$ is sufficiently large, all the liquid is within the mesh cylinder. If $F_{\sigma\tilde{k}}$ is not large enough, most of the liquid is within the mesh cylinder but part of liquid still settles on the tube bottom.

The heat transfer enhancement is related to the phase distribution. Fig. 6a shows the cross-section in the bare tube. The heat transfer rate per unit flow length is

$$Q_{BT} = h_{film}\cdot\Delta T\cdot S_v \tag{25}$$

where $h_{film}$ is the thin film condensation heat transfer coefficient, $\Delta T$ is the temperature difference between the vapor and the tube wall and $S_v$ is the circumference length exposed by vapor. When the liquid height is $\tilde{h}_l$ (see Fig. 6a), $S_v$ is

$$S_v = \pi d_{ins} - d_{ins}\cdot\arccos\left(1 - 2\tilde{h}_l/d_{ins}\right) \tag{26}$$

Fig. 6b shows the liquid height $\tilde{h}_l$ modulated by the mesh cylinder, in which $\tilde{h}_{min}$ and $\tilde{h}_{max}$ are liquid levels that contact with the mesh cylinder bottom and top, respectively. An ideal case is that all the liquid is within the mesh cylinder (see Fig. 6c). The heat transfer rate per unit flow length becomes

$$Q_{MHTT} = h_{film}\cdot\Delta T\cdot S \tag{27}$$

where $S$ is the tube circumference ($S = \pi d_{ins}$). By comparing Eqs. (25) and (27), the heat transfer enhancement ratio is

$$EF = \frac{Q_{MHTT}}{Q_{BT}} = \frac{S}{S_v} = \frac{1}{1 - \arccos\left(1 - 2\tilde{h}_l/d_{ins}\right)/\pi} \tag{28}$$

Substituting $\tilde{h}_{min} = 1.81$ mm and $\tilde{h}_{max} = 13.01$ mm in this study, the heat transfer enhancement ratio reached $1.29 \le EF \le 3.62$. The phase distribution in Fig. 5 was verified by our previous observations for the air–water flow experiment, in which a hollow mesh cylinder was inserted in a long glass tube [16]. The numerical simulation for the air–water flow pattern modulation [17] also supported the phase structure shown in Fig. 5. Because the surface tension force for R123 is smaller than that for air–water system, more fine mesh pores were used in this study. In other

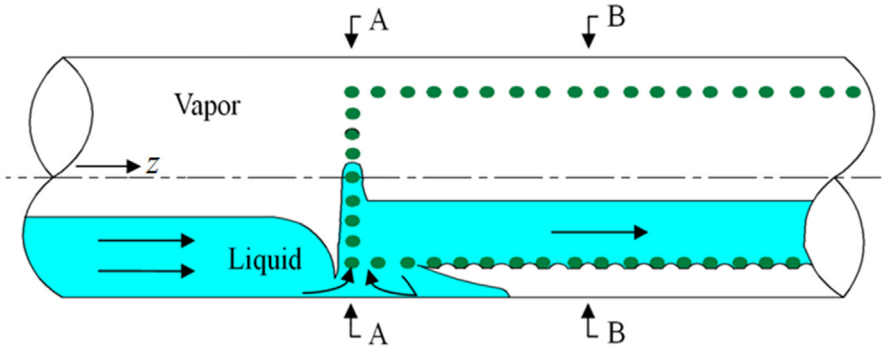


(a) Phase distribution of the stratified flow in bare tube region and flow pattern modulation region

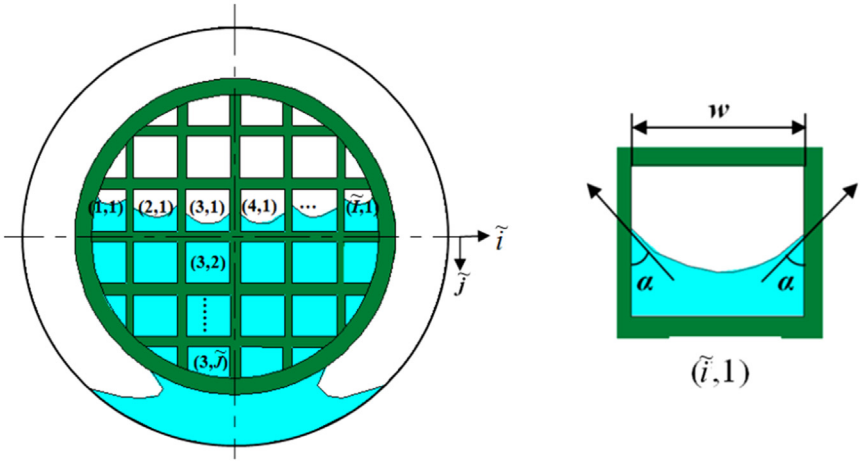


(b) Phase distribution and force analysis over the A-A cross section

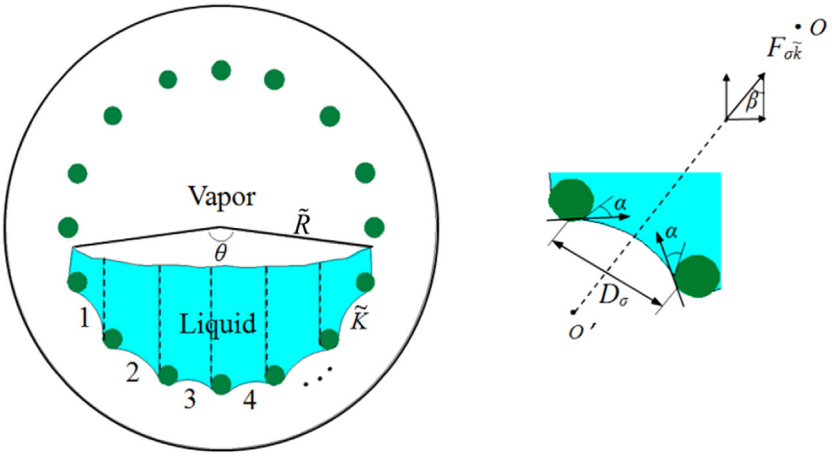


(c) Phase distribution and force analysis over the B-B cross section

**Fig. 5.** The stratified flow and its interaction with the mesh cylinder.

words, the R123 condensation flow system can be analogical to the air–water flow system if one matches the surface tension force with the mesh pore size. Fig. 5 shows the phase distribution, reflecting the static force balance, qualitatively.

*3.1.3. Annular flow pattern modulation analysis*

Annular flow contains the vapor core in the tube and liquid film on the tube wall. Liquid droplets are entrained in the vapor core [27]. The high-speed camera was combined with a microscope to observe the droplet capture process by the mesh screen surface. The mesh screen surface was put under the microscope. Fig. 7 shows an R123 droplet spreading on the mesh screen surface. The initial droplet diameter was about 1.15 mm. The droplet was above the mesh surface at $t = 0$, but it contacted with the mesh surface at $t = 2.5$ ms. Then, the droplet was quickly spreading and penetrating the mesh pores. The wetting area was increased in a circular shape (see images for 2.5 ms $< t <$ 7.5 ms). A wetting area by 2.12 mm and 1.88 mm was formed finally, in which the mesh

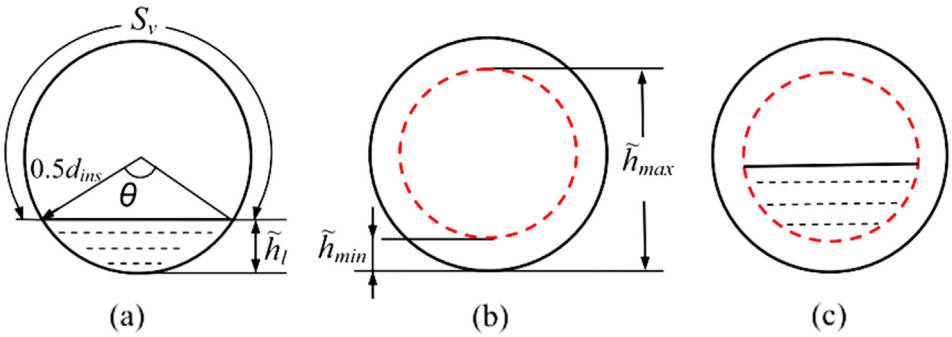


**Fig. 6.** The geometry configuration for the estimate of the heat transfer enhancement ratio (a for the bare tube cross-section; b for the minimum and maximum liquid heights with mesh cylinder insert; and c for the liquid within the mesh cylinder).

pores were filled with liquid with gas–liquid interfaces exposed in the ambient air. Other droplet sizes larger or smaller than that shown in Fig. 7 were also tried. The droplet spreading process was similar to that shown in Fig. 7. The difference was only the spreading time. Thus, the mesh screen surface could be treated as a completely hydrophilic surface with the contact angle of 0°.

If the mesh cylinder was dry, flushing the system with the liquid ensured the mesh pores occupied by liquid. When an annular flow interacted with the micro-membrane surface, liquid droplets were captured by the surface. The liquid flowing toward the mesh cylinder decreased the liquid content near the tube wall. Thus, the vapor void fractions near the tube wall were increased to enhance the heat transfer.

### 3.2. Heat transfer measurement

During the phase change process, parameters may be oscillating versus time due to the two-phase flow instability. An orifice restrictor was put at the evaporator inlet so that the two-phase flow instability was suppressed to reach the quasi-steady operation. Fig. 8 shows the repeatable two-phase measurements for $G = 200$ kg/m$^2$s and $x_{in} = 0.195$. The black and red curves were obtained on the first and second days, respectively. It is seen that the test was repeatable. The inlet and outlet cooling water temperatures were very stable. Even though small two-phase oscillation existed in the system, the wall temperatures $T_{4,w,s}$ (cross-section 4 and side wall location) was oscillating in a narrow range of less than 0.2–0.3 °C. This was because the thermal inertia of the copper tube wall further flattened the temperature oscillations. All the 21 wall temperatures were involved in the heat transfer coefficient computation, and the data was averaged over a longer time period of several minutes. The hardware arrangement and data processing procedure ensured the experimental data reliability.

The BT and MHTT data constructed a pair of cases, for which R123 had almost the same $G$ and $x_{in}$. The cooling water also had the same $m_c$ and $T_{c,in}$. This operating procedure caused different R123 outlet vapor mass qualities ($x_{out}$) and outlet temperatures of the cooling water ($T_{c,out}$). Fig. 9 shows the top, side and bottom wall temperatures over the seven cross-sections.

Fig. 9a demonstrates the negative $x_{out}$ (the outlet subcooled liquid). The flow length was divided into a condensation flow part for $0 < x < x_{in}$ and a liquid flow part for $x_{out} < x < 0$, interfaced at $x_{eq} = 0$, where $x_{eq}$ is the thermodynamic equilibrium vapor quality. Thus, the MCLF (mixed condensation and liquid flow) is called. Fig. 9a shows that the MHTT increased wall temperatures in the condensation flow part to indicate the enhanced condensation heat

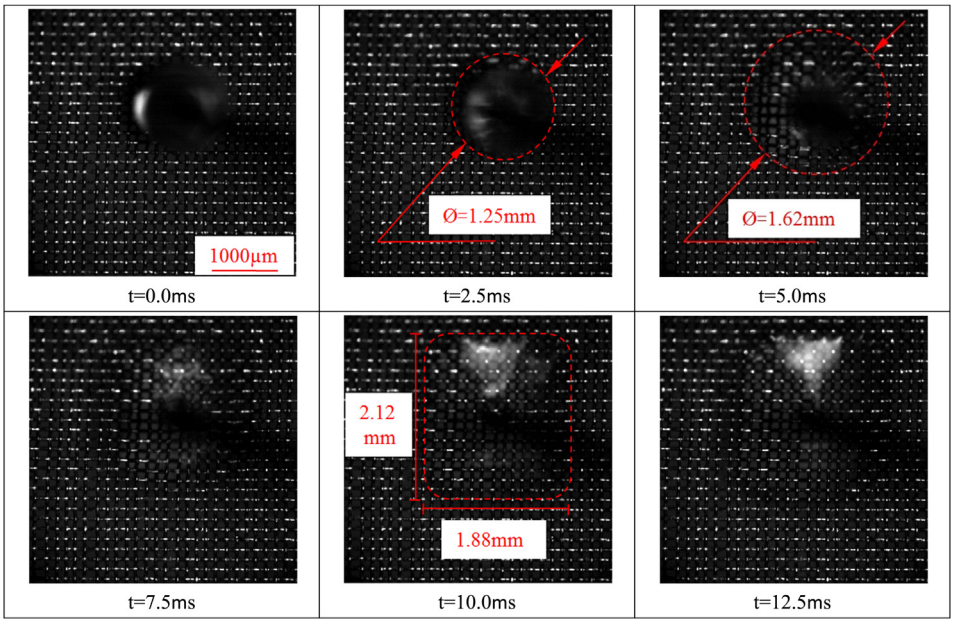


**Fig. 7.** The high-speed observation of a R123 liquid droplet spreading process on the mesh screen surface.

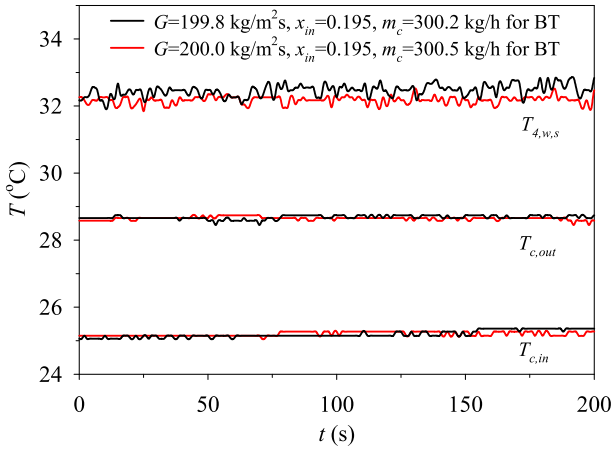


**Fig. 8.** Repeatable experiment for a typical case (the black curves were obtained on the first day; the red curves were obtained on the second day). (For interpretation of the references to color in this figure legend, the reader is referred to the web version of this article.)

transfer. However, the MHTT decreased the wall temperatures in the liquid flow part to indicate the deteriorated heat transfer. The comprehensive effect yielded almost the same temperature rise of the cooling water in the tube annulus: 3.5 °C for the MHTT and 3.3 °C for the BT.

Fig. 9b shows wall temperatures with $G \approx 200$ kg/m$^2$s, $x_{in} \approx 0.49$ and $m_c \approx 300$ kg/h. Fig. 9c plots the data with $x_{in}$ up to 0.92. The $x_{out}$ values were positive, indicating the condensation flow along the whole flow length. Thus, the PCF (pure condensation flow) is called. The MHTT obviously increased wall temperatures. The enhanced condensation heat transfer increased the heat transfer rate. For instance, Fig. 9c gives the temperature rises of the cooling water by 7.6 °C for the MHTT and 6.7 °C for the BT, yielding about 14.3% increase of the heat transfer rate.

Fig. 10 shows the condensation heat transfer coefficients, $h$, against the inlet vapor mass qualities, $x_{in}$, with $G = 200$–$500$ kg/m$^2$s and $m_c = 300$ kg/h. The MHTT had larger $h$ than the BT. The heat transfer enhancement ratios (EF) were larger than one. There was a minimum EF point corresponding to the MCLF case. The deteriorated liquid heat transfer suppressed the increment of heat transfer enhancement ratios. The minimum EF point occurred at $x_{in} \approx 0.1$ with $G = 400$–$500$ kg/m$^2$s (see Fig. 10a–b), but it was shifted to $x_{in} \approx 0.2$ with $G = 200$ kg/m$^2$s (see Fig. 10d). For the PCF cases (condensation flow in the whole tube length), EF was increased with mass fluxes and inlet vapor mass qualities. The EF values were in the range of 1.18–2.12, with the maximum EF occurring at $G = 500$ kg/m$^2$s and $x_{in} = 0.299$.

EF was increased with $G$ and $x_{in}$. Here $h$ and EF were plotted versus $Gx_{in}$ (vapor mass flux). Fig. 11a shows the increase trend of $h$ with $Gx_{in}$ for both BT and MHTT. The MHTT attained the maximum $h$ of 5.40 kW/m$^2$K at $Gx_{in} = 149$ kg/m$^2$s. Fig. 11b displays the increased EF with $Gx_{in}$, except for $Gx_{in} < 50$ kg/m$^2$s. The minimum EF occurred at $Gx_{in} \approx 50$ kg/m$^2$s, corresponding to the MCLF case. Other data points beyond the minimum point were the PCF cases.

Fig. 12 shows the thermal resistances with $G = 400$ kg/m$^2$s, $m_c = 700$ and 300 kg/h. The wall thermal resistance, $R_w$, contributed less and could be neglected. The condensation thermal resistance, $R_r$, was significantly larger than the cooling water resistance, $R_c$. The total thermal resistances, $R_{to} = R_r + R_w + R_c$, were decreased with increases in $x_{in}$ for both BT and MHTT. The MHTT obviously decreased $R_r$. With $G = 400$ kg/m$^2$s, $x_{in} = 0.045$ and $m_c = 300$ kg/h, the BT had $R_r$ of 26.43 K/kW, but the MHTT had $R_r$ of 17.11 K/kW to have 35.0% reduction compared with the BT (see Fig. 12b). The

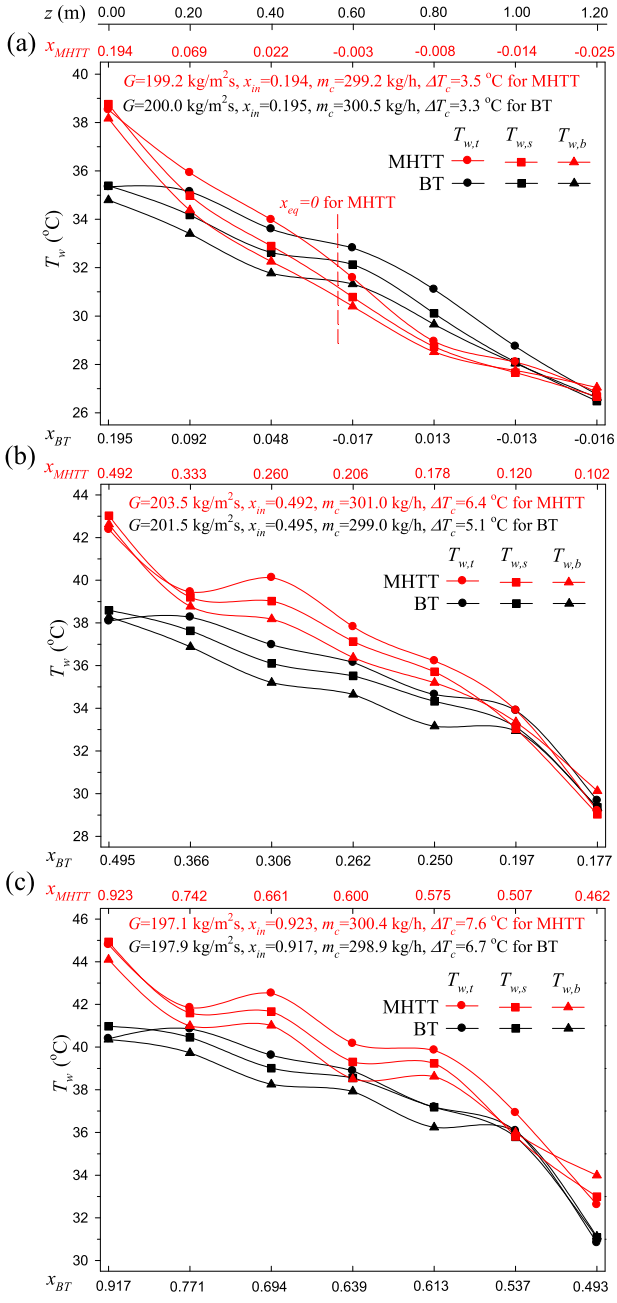


**Fig. 9.** The measured copper wall temperatures for the BT and MHTT.

MHTT decreased the total thermal resistance by 31.8% for this case. The MHTT decreased the total thermal resistance by 45.6% maximally, occurring at $G = 200$ kg/m$^2$s, $x_{in} = 0.101$ and $m_c = 700$ kg/h. Even though the heat transfer enhancement ratios were large at high inlet vapor qualities, the MHTT was more effective to decrease the total thermal resistance at low vapor qualities. This is because the thermal resistance was much large at low vapor qualities. Fig. 12 shows that the flow rates of the cooling water had less influence on the total thermal resistances.

### 3.3. Explanation of the observed phenomenon

#### 3.3.1. MCLF cases

Fig. 13a shows the MCLF case. The tube length was divided into a condensation part, $L_{TP}$, and a liquid part, $L_{SP}$, interfaced at $x_{eq} = 0$.

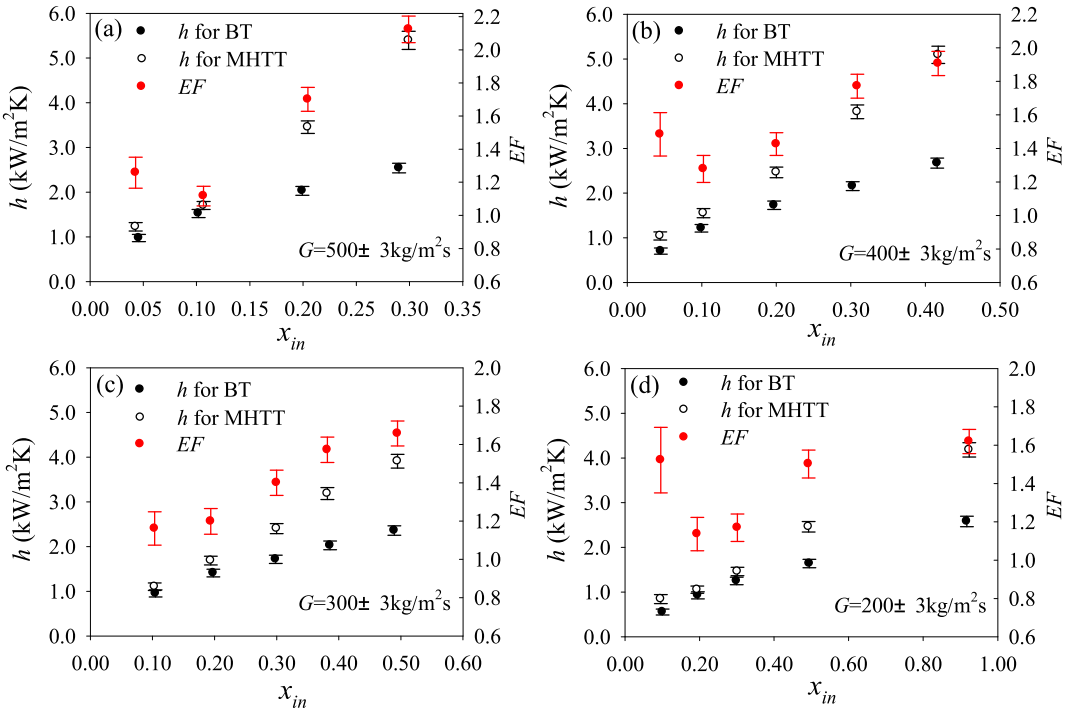


**Fig. 10.** The heat transfer coefficients for the BT and MHTT and the heat transfer enhancement ratios at $m_c$ = 300 kg/h.

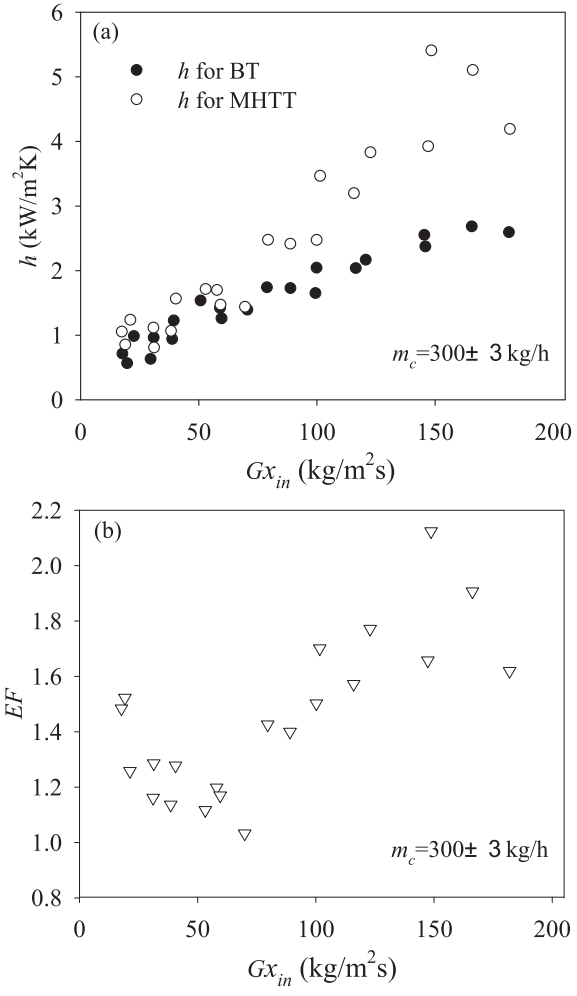


**Fig. 11.** Heat transfer coefficients for the BT and MHTT and heat transfer enhancement ratios (data plotted versus $Gx_{in}$).

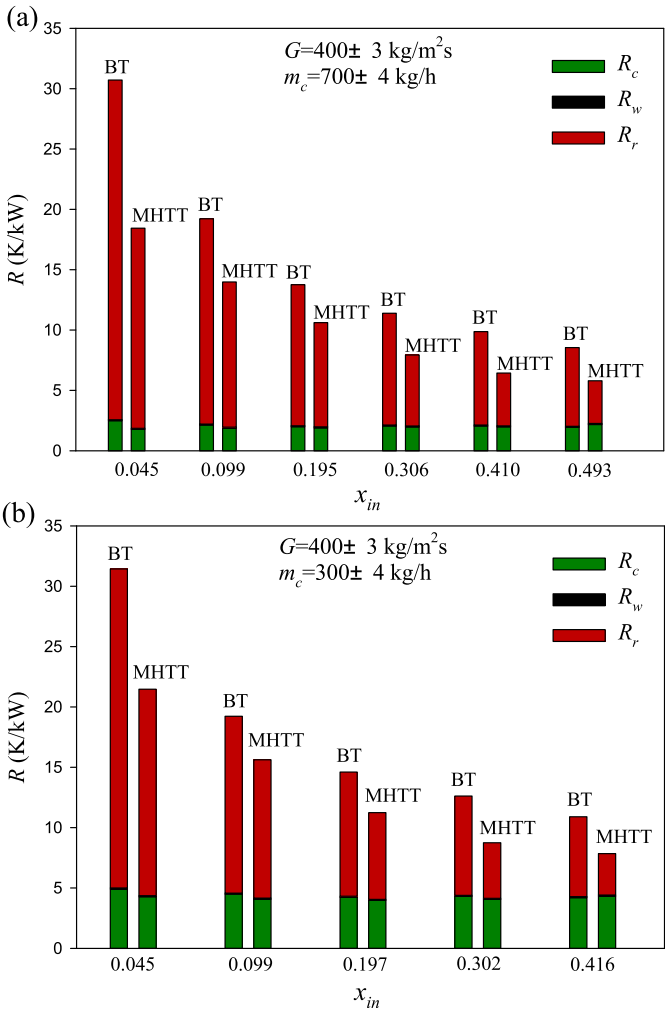


**Fig. 12.** Thermal resistances versus $x_{in}$ at two flow rates of the cooling water.

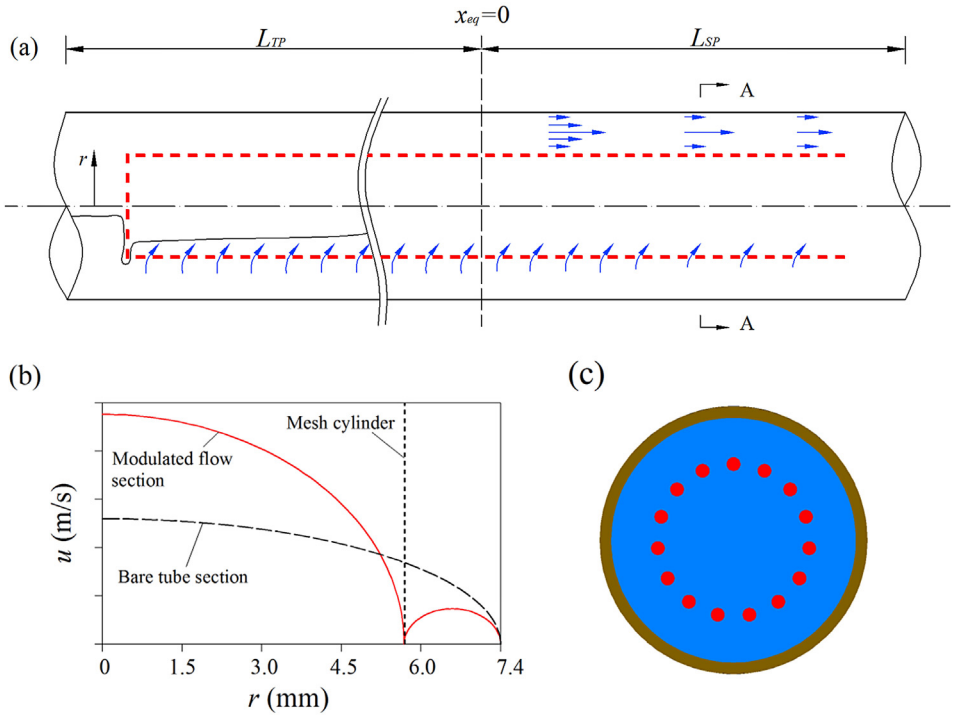


**Fig. 13.** The flow picture for the MCLF cases.

The condensation part involved the modulated SS or SW flow. The increased vapor covered tube wall surface contributed the heat transfer enhancement. The mesh cylinder held a higher liquid level in the core region and decreased the liquid level in the annular region (see Fig. 4). The situation was changed for the single-phase liquid flow. Cao et al. [28] showed the significant heat transfer enhancement with short mesh cylinders. A longer mesh cylinder such as encountered in this study deteriorated the convective heat transfer. Fig. 13b shows the axial velocity over the radial direction, qualitatively. The bare tube behaved large velocity at the tube center and decreased velocity near the tube wall. The MHTT caused the radial flow from the annular region to the core region. A longer section to keep the radial flow decreased the axial velocity and its gradient near the tube wall (see the red curve in Fig. 13b), deteriorating the convective heat transfer. (For interpretation of the references to color in this figure, the reader is referred to the web version of this article.) The comprehensive effect suppressed the increment of heat transfer enhancement ratios, which were about 1.1–1.3 with $Gx_{in}$ = 30–60 kg/m$^2$s (see Fig. 11). Thus, the outlet over-subcooled liquid cases are not recommended. Instead, the saturated or slightly subcooled liquid cases at the outlet are perfect.

### 3.3.2. PCF cases

The annular flow occurred with increases in $G$ or $x_{in}$, under which $h$ and EF were increased with $Gx_{in}$. Fig. 14 marks four pressures. $P_{e,an}$ and $P_{e,co}$ were the exit pressures in the annular region and the core region, respectively. $P_{u,an}$ and $P_{u,co}$ were the upstream pressures in the annular region and the core region, respectively. Because the two fluid streams from the annular region and the core region mixed at the tube exit, it is reasonable to assume $P_{e,an} \approx P_{e,co}$.

$P_{u,co} - P_{e,co}$ is the liquid frictional pressure drop in the core region:

$$\Delta P_{f,co} = P_{u,co} - P_{e,co} \tag{29}$$

For the two-phase flow in the annular region, the following equation describes $P_{u,an}$ and $P_{e,an}$:

$$P_{u,an} - P_{e,an} = \Delta P_{f,an}\phi_{lo}^2 \tag{30}$$

where $\Delta P_{f,an}$ is the frictional pressure drop assuming the total two-phase mixture in the annular region flowing as liquid alone, and $\phi_{lo}^2$ is the two-phase multiplier having the range of 10–100. Combining Eqs. (29) and (30) yields

$$P_{u,an} - P_{u,co} = P_{e,an} - P_{e,co} + \Delta P_{f,an}\phi_{lo}^2 - \Delta P_{f,co} \approx \Delta P_{f,an}\phi_{lo}^2 - \Delta P_{f,co} \tag{31}$$

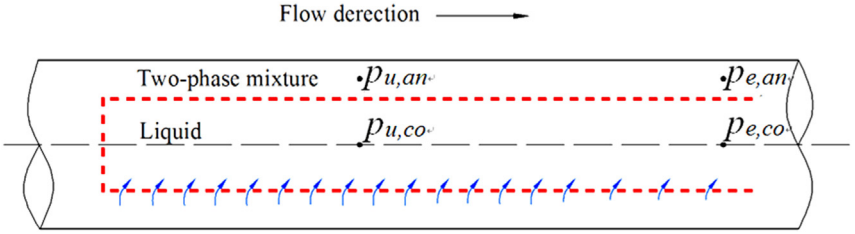


**Fig. 14.** The four pressures marked for the PCF cases.

$P_{u,an} - P_{u,co}$ is the pressure difference across the micro-membrane surface, which is the driving force for the liquid flowing from the annular region to the core region. Eq. (31) indicates that $P_{u,an} - P_{u,co}$ consumes much percentage of the two-phase frictional pressure drop due to$\Delta P_{f,co} \ll \Delta P_{f,an}\phi_{lo}^2$.

The increased $Gx_{in}$ raises the two-phase frictional pressure drop. Thus, the pressure difference across the mesh screen surface is increased. This causes more liquid flowing from the annular region to the core region to increase the near-wall vapor void fractions, increasing the heat transfer enhancement ratios.

### 3.4. Penalty of the pressure drop increase

The enhanced condensation heat transfer accompanied the frictional pressure drop increase (see Fig. 15a). The BT slightly increased $\Delta P_f$ with $Gx_{in}$. The MHTT had larger slopes of $\Delta P_f$ versus $Gx_{in}$ than the BT, noting that $m_c$ had less influences on $\Delta P_f$ for both tubes.

The heat transfer device is recommended to be used if PEC > 1. The larger the PEC number, the better the heat transfer device is. Fig. 15b shows PEC, displaying the quasi-parabola distribution versus $Gx_{in}$. There were 42 data points having PEC > 1 and the maximum PEC attained 1.7. There were 14 data points having PEC < 1 with $Gx_{in}$ = 30–60 kg/m$^2$s for $x_{out} < 0$, caused by the suppression of the heat transfer enhancement ratios. This is a preliminary modulated heat transfer study. There are many parameters involved in the MHTT. The MHTT optimization is expected. The complicated flow and heat transfer mechanisms should be further explored for low-grade energy utilizations.

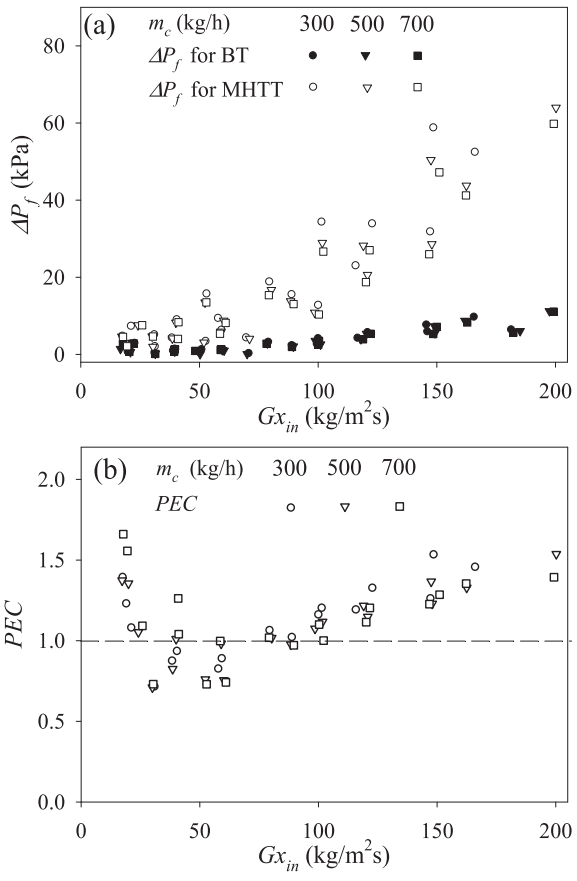


**Fig. 15.** Frictional pressure drops for the BT and MHTT and the PEC numbers versus $Gx_{in}$.

## 4. Conclusions

Major conclusions are summarized as follows.

- The 76 μm-mesh-pore surface modulated the stratified flows, effectively. Most of the liquid was within the mesh cylinder. Thus, the vapor covered tube wall surface was increased to enhance the heat transfer.
- The mesh cylinder effectively modulated the annular flows. Liquid droplets in the vapor core were quickly captured by the mesh screen surface, causing the liquid flow from the annular region to the core region to increase the near-wall vapor void fractions.
- The measurements showed the heat transfer enhancement ratios covering the range of 1.18–2.12. The total thermal resistances were decreased by 45.6%, maximally.
- For the MCLF cases, the increment of heat transfer enhancement ratios was suppressed due to the deteriorated heat transfer in the liquid flow section.
- For the PCF cases, the heat transfer enhancement ratios were increased with the vapor mass fluxes, $Gx_{in}$. The increased $Gx_{in}$ raised the frictional two-phase pressure drop in the annular region. Thus, the pressure difference across the micro-membrane surface was raised to push more liquid flowing toward the core region.
- The PEC numbers were larger than one for 42 data points corresponding to the PCF cases. They were less than one for 14 data points corresponding to the MCLF cases.

## Acknowledgments

This work was supported by the National Natural Science Foundation of China of International cooperation project (51210011), the National Basic Research Program of China (2011CB710703), and the National Natural Science Foundation of China project (U1034004).

## References

[1] Dewan A, Mahanta P, Raju KS, Kumar PS. Review of passive heat transfer augmentation techniques. Proc Inst Mech Eng Part A-J Power Energy 2004;218(7):509–27.
[2] Zhou N, Wang X, Chen Z, Wang Z. Experimental study on organic Rankine cycle for waste heat recovery from low-temperature flue gas. Energy 2013;55:216–25.
[3] Larsen U, Pierobon L, Haglind F, Gabrielii C. Design and optimisation of organic Rankine cycles for waste heat recovery in marine applications using the principles of natural selection. Energy 2013;55:803–12.
[4] Khatita MA, Ahmed TS, Ashour FH, Ismail IM. Power generation using waste heat recovery by organic Rankine cycle in oil and gas sector in Egypt: a case study. Energy 2014;64:462–72.
[5] Chen H, Goswami DY, Rahman MM, Stefanakos EK. A supercritical Rankine cycle using zeotropic mixture working fluids for the conversion of low-grade heat into power. Energy 2011;36(1):549–55.
[6] Han W, Sun L, Zheng D, Jin H, Ma S, Jing X. New hybrid absorption–compression refrigeration system based on cascade use of mid-temperature waste heat. Appl Energy 2013;106:383–90.
[7] Kwon O, Cha D, Park C. Performance evaluation of a two-stage compression heat pump system for district heating using waste energy. Energy 2013;57:375–81.
[8] Kato Y, Sasaki Y, Yoshizawa Y. Magnesium oxide/water chemical heat pump to enhance energy utilization of a cogeneration system. Energy 2005;30(11):2144–55.
[9] Heat and transfer solution: heat transfer coefficients; November 07, 2008. http://www.hcheattransfer.com/coeffic -ents.html.
[10] Graham D, Chato JC, Newell TA. Heat transfer and pressure drop during condensation of refrigerant 134a in an axially grooved tube. Int J Heat Mass Transfer 1998;42(11):1935–44.
[11] Cavallini A, Del Col D, Doretti L, Longo GA, Rossetto L. Heat transfer and pressure drop during condensation of refrigerants inside horizontal enhanced tubes. Int J Refrig 2000;23(1):4–25.
[12] Miyara A, Otsubo Y. Condensation heat transfer of herringbone micro fin tubes. Int J Therm Sci 2002;41(7):639–45.

[13] Laohalertdecha S, Wongwises S. Condensation heat transfer and flow characteristics of R-134a flowing through corrugated tubes. Int J Heat Mass Transfer 2011;54(11):2673–82.
[14] Nitheanandan T, Soliman HM. Influence of tube inclination on the flow regime boundaries of condensing steam. Can J Chem Eng 1993;71(1):35–41.
[15] Lips S, Meyer JP. Stratified flow model for convective condensation in an inclined tube. Int J Heat Fluid Flow 2012;36:83–91.
[16] Chen H, Xu J, Li Z, Xing F, Xie J, Wang W, et al. Flow pattern modulation in a horizontal tube by the passive phase separation concept. Int J Multiph Flow 2012;45:12–23.
[17] Chen Q, Xu J, Sun D, Cao Z, Xie J, Xing F. Numerical simulation of the modulated flow pattern for vertical upflows by the phase separation concept. Int J Multiph Flow 2013;56:105–18.
[18] Tropea C, Yarin AL, Foss JF. Handbook of experimental fluid mechanics, vol. 1. Springer; 2007.
[19] Dittus FW, Boelter LMK. Heat transfer in automobile radiators of the tubular type. Int Commun Heat Mass Transfer 1985;12(1):3–22.
[20] Zhang X, Liu Z, Liu W. Numerical studies on heat transfer and flow characteristics for laminar flow in a tube with multiple regularly spaced twisted tapes. Int J Therm Sci 2012;58:157–67.
[21] Fan JF, Ding WK, Zhang JF, He YL, Tao WQ. A performance evaluation plot of enhanced heat transfer techniques. Int J Heat Mass Transfer 2009;52(1):33–44.
[22] Tran TN. Pressure drop and heat transfer study of two-phase flow in small channels. Ph.D. dissertation. Texas: Texas Tech University; 1998.
[23] Holman JP, Gajda WJ. Experimental methods for engineers. 4th ed. Nueva York: McGraw-Hill; 1994.
[24] Breber G, Palen JW, Taborek J. Prediction of horizontal tube-side condensation of pure components using flow regime criteria. J Heat Transfer 1980;102:471–6.
[25] Tandon TN, Varma HK, Gupta CP. A new flow regime map for condensation inside horizontal tubes. J Heat Transfer 1982;104:763–8.
[26] Hajal JE, Thome JR, Cavallini A. Condensation in horizontal tubes, part 1: two-phase flow pattern map. Int J Heat Mass Transfer 2003;46(18):3349–63.
[27] Simmons MJH, Hanratty TJ. Droplet size measurements in horizontal annular gas-liquid flow. Int J Multiph Flow 2001;27(5):861–83.
[28] Cao Z, Xu J, Sun D, Xie J, Xing F, Chen Q, et al. Numerical simulation of modulated heat transfer tube in laminar flow regime. Int J Therm Sci 2014;75:171–83.